

Near-polytropic simulations with a radiative surface

A. Barekat^{1,2} and A. Brandenburg^{1,2}

¹ Nordita, KTH Royal Institute of Technology and Stockholm University, Roslagstullsbacken 23, 10691 Stockholm, Sweden

² Department of Astronomy, AlbaNova University Center, Stockholm University, 10691 Stockholm, Sweden

August 8, 2013, Revision: 1.86

ABSTRACT

Context. Studies of solar and stellar convection often employ simple polytropic setups using the diffusion approximation instead of solving the proper radiative transfer equation. This allows one to control separately the polytropic index of the hydrostatic reference solution, the temperature contrast between top and bottom, and the Rayleigh and Péclet numbers.

Aims. Here we extend such studies by including radiative transfer in the gray approximation using a Kramers-like opacity with freely adjustable coefficients. We study the properties of such models and compare with results from the diffusion approximation.

Methods. We use the PENCIL CODE, which is a high-order finite difference code where radiation is treated using the method of long characteristics. The source function is given by the Planck function. The opacity is written as $\kappa = \kappa_0 \rho^a T^b$, where $a = 1$ in most cases, b is varied from -3.5 to $+5$, and κ_0 is varied by four orders of magnitude. We adopt a perfect monatomic gas. We consider sets of one-dimensional models and perform a comparison with the diffusion approximation in a two-dimensional model.

Results. Except for the case with $b = 5$, we find one-dimensional hydrostatic equilibria with a nearly polytropic stratification and a polytropic index close to $n = (3 - b)/(1 + a)$, covering both convectively stable ($n > 3/2$) and unstable ($n < 3/2$) cases. For $b = 3$ and $a = -1$, the value of n is undefined, but the final equilibrium stratification turns out to be nearly isentropic. For large values of κ_0 , the thermal adjustment time becomes long, the Péclet and Rayleigh numbers become large, and the temperature contrast increases and is thus no longer an independent input parameter, unless the Stefan–Boltzmann constant is considered adjustable.

Conclusions. Proper radiative transfer with Kramers-like opacities provides a useful tool for studying stratified layers with a radiative surface in ways that are more physical than what is possible with polytropic models using the diffusion approximation.

Key words. Radiative transfer – hydrodynamics – Sun: atmosphere

1. Introduction

Convection in stars and accretion discs is a consequence of radiative cooling at the surface. Pioneering work by Nordlund (1982, 1985) has shown that realistic simulations of solar granulation can be performed with not too much extra effort and the required computing resources are comparable to the mandatory costs for solving the hydrodynamics part. Yet, many studies of hydrodynamic and hydromagnetic convection today ignore the effects of proper radiative transfer—sometimes even at the expense of using compute-intensive implicit solvers to cope with a computationally stiff problem in the upper layers where the radiative conductivity becomes large (e.g. Cattaneo et al., 1991; Gastine & Dintrans, 2008). Therefore, the main reason for ignoring radiation cannot be just the extra effort, but it is more likely a reduced flexibility in that one is confined to a single physical realization of a system and the difficulty in varying parameters that are in principle fixed by the physics. With only a few exceptions (e.g. Edwards, 1990), radiation hydrodynamics simulations of stratified convection also employ realistic opacities combined with a realistic equation of state. In the case of the Sun this means that one can only simulate for the duration of a few days solar time (Stein & Nordlund, 1989, 1998, 2012).

There are other types of realistic simulations that are able to cover longer time scales by simulating only deeper layers, so they ignore radiation. However, such simulations still need to pose an upper boundary condition, where the gas is cooled (Miesch et al., 2000). This leads to a granulation-like pattern at a depth where the flow topology is known to consist of individual downdrafts rather than a connected network of intergran-

ular lanes. This compromises the realism of such simulations. Other types of simulations give up the ambition for realism altogether and try to model a “toy Sun” in which the broad range of time and length scales is compressed to a much narrower range (Käpylä et al., 2013). This can be useful if one wants to understand the physics of the solar dynamo, where we are not even sure about the possible importance of the surface (Brandenburg, 2005), or the physics of sunspots, where so far only models of a toy Sun have produced spontaneous magnetic flux concentrations similar to those of sunspots (Brandenburg et al., 2013). It is therefore important to know how to manipulate the parameters to accommodate the relevant physics, given certain numerical constraints such as the number of mesh points available.

In the present paper we include radiation, which introduces the Stefan–Boltzmann constant, σ_{SB} , as a new characteristic quantity into the problem. It characterizes the strength of surface cooling, or, conversely, the temperature needed to radiate the flux that is transported through the rest of the domain. Earlier simulations that ignored radiation have specified the surface temperature in an ad hoc manner so as to achieve a certain temperature contrast across the domain. An example are the simulations of Brandenburg et al. (1996), who specified a parameter ξ as the ratio of pressure scale height at the surface, which is proportional to the temperature at the top, and the thickness of the convectively unstable layer. Alternatively, one can use a radiative surface boundary condition. It involves σ_{SB} and couples therefore the surface temperature T_{top} to the lower part of the system, so T_{top} is then no longer a free parameter, unless one chooses an effective value of σ_{SB} such as to achieve the desired temperature

contrast. This was done in recent simulations by Käpylä et al. (2012), who kept the aforementioned parameter ξ as the basic control parameter, which then determines the effective value of σ_{SB} in their simulations.

The goal of the present work is to explore the physics of models that introduce radiation without being confined to just one realization. We do this by using a Kramers-like opacity law, but with freely adjustable parameters. It turns out that it is in some cases possible to imitate polytropic models with any desired polytropic index and Rayleigh number. This then eliminates any restrictions to a single setup, allowing one to perform parameter surveys, just like with earlier polytropic models. To compare radiative transfer models with those in the diffusion approximation, we consider two-dimensional convection simulations.

We begin by presenting first the governing equations and then describe the basic setup of our model. Next we compare a set of one-dimensional simulations with the associated polytropic indices that correspond to Schwarzschild stable or unstable solutions. Finally, we explore the effect of including radiative transfer instead of using the diffusion approximation combined with a radiative boundary condition by comparing two-dimensional simulations.

2. The model

2.1. Governing equations

We solve the hydrodynamics equations for logarithmic density $\ln \rho$, velocity \mathbf{u} , and specific entropy s , in the form

$$\frac{D \ln \rho}{Dt} = -\nabla \cdot \mathbf{u}, \quad (1)$$

$$\rho \frac{D \mathbf{u}}{Dt} = -\nabla p + \rho \mathbf{g} + \nabla \cdot (2\rho \nu \mathbf{S}), \quad (2)$$

$$\rho T \frac{Ds}{Dt} = -\nabla \cdot \mathbf{F}_{\text{rad}} + 2\rho \nu \mathbf{S}^2, \quad (3)$$

where p is the gas pressure, T is the temperature, \mathbf{g} is the gravitational acceleration, \mathbf{F}_{rad} is the radiative flux, $\mathbf{S} = \frac{1}{2}[\nabla \mathbf{u} + (\nabla \mathbf{u})^T] - \frac{1}{3}\mathbf{I}\nabla \cdot \mathbf{u}$ is the traceless rate of strain tensor, where \mathbf{I} is the unit tensor, and ν is the viscosity. For the equation of state, we assume a perfect gas with $p = (\mathcal{R}/\mu)T\rho$, where \mathcal{R} is the universal gas constant and μ is the mean molecular weight. The pressure is related to s via $p = \rho^\gamma \exp(s/c_v)$, where the adiabatic index $\gamma = c_p/c_v$ is the ratio of specific heats at constant pressure and constant volume, respectively, and $c_p - c_v = \mathcal{R}/\mu$. To obtain the radiative flux, we adopt the gray approximation, ignore scattering, and assume that the source function S (not to be confused with the rate of strain tensor \mathbf{S}) is given by the frequency-integrated Planck function, so $S = (\sigma_{\text{SB}}/\pi)T^4$, where σ_{SB} is the Stefan–Boltzmann constant. The divergence of the radiative flux is then given by

$$\nabla \cdot \mathbf{F}_{\text{rad}} = -\kappa \rho \oint_{4\pi} (I - S) d\Omega, \quad (4)$$

where κ is the opacity per unit mass (assumed independent of frequency) and $I(\mathbf{x}, t, \hat{\mathbf{n}})$ is the frequency-integrated specific intensity corresponding to the energy that is carried by radiation per unit area, per unit time, in the direction $\hat{\mathbf{n}}$, through a solid angle $d\Omega$. We obtain $I(\mathbf{x}, t, \hat{\mathbf{n}})$ by solving the radiative transfer equation,

$$\hat{\mathbf{n}} \cdot \nabla I = -\kappa \rho (I - S), \quad (5)$$

along a set of rays in different directions $\hat{\mathbf{n}}$ using the method of long characteristics.

2.2. Opacity

For our work it is essential that we can control the value and functional form of the opacity. We therefore choose a Kramers-like opacity given by

$$\kappa = \kappa_0 \rho^a T^b, \quad (6)$$

where a and b are free parameters that characterize the relevant radiative processes. It is useful to consider the radiative conductivity $K(\rho, T)$, which is given by

$$K(\rho, T) = \frac{16\sigma_{\text{SB}}T^3}{3\kappa\rho} = \frac{16\sigma_{\text{SB}}T^{3-b}}{3\kappa_0\rho^{a+1}}. \quad (7)$$

Note that, in a plane-parallel polytropic atmosphere, $T(z)$ varies linearly with height z and in the stationary state, $K(\rho, T)$ is constant in the optically thick part. This implies that ρ is proportional to T^n , where

$$n = \frac{3-b}{1+a} \quad (8)$$

is the polytropic index (not to be confused with the direction of the ray $\hat{\mathbf{n}}$). This relation was also used by Edwards (1990), but the author regarded those solutions are ‘a little contrived’. This is perhaps the case if such solutions are applied throughout the entire domain. It should also be noted that Edwards (1990) included thermal conduction along with radiative transfer. This meant that one had to pose a boundary condition for the temperature at the top also, which will not be necessary in our case, where, unless states otherwise, no thermal conductivity is included. Indeed, as we shall show, with a Kramers-like opacity, nearly polytropic solutions are a natural outcome in the lower optically thick part of the domain, while in the upper optically thin part of the domain the stratification tends to become approximately isothermal.

For a perfect gas, the specific entropy gradient is related to the gradients of the other thermodynamic variables via

$$\nabla s = c_v \nabla \ln p - c_p \nabla \ln \rho = (n+1-\gamma n)c_v \nabla \ln T, \quad (9)$$

and vanishes when $n = 1/(\gamma - 1)$. For a monatomic gas where $\gamma = 5/3$, the stratification is Schwarzschild-stable for $n > 3/2$.

2.3. Boundary conditions

We consider a slab with boundary conditions in the z direction at z_{bot} and z_{top} , where we assume the gas to be stress-free, i.e.,

$$\partial u_x / \partial z = \partial u_y / \partial z = u_z = 0 \quad \text{on } z = z_{\text{bot}}, z_{\text{top}}. \quad (10)$$

We assume zero incoming intensity at the top, and compute the incoming intensity at the bottom from a quadratic Taylor expansion of the source function, which implies that the diffusion approximation is obeyed; see Appendix A of Heinemann et al. (2006) for details. To ensure steady conditions, we fix temperature at the bottom,

$$T = T_0 \quad \text{on } z = z_{\text{bot}}, \quad (11)$$

while the temperature at the top is allowed to evolve freely. There is no boundary condition on the density, but since no mass is flowing in or out, the volume-averaged density is automatically constant. Since most of the mass resides near the bottom, the density there will not change drastically and will be close to its initial value at the bottom, ρ_0 .

2.4. The radiation module

We use for all simulations the PENCIL CODE¹, which solves the hydrodynamic differential equations with a high-order finite-difference scheme. The radiation module was implemented by Heinemann et al. (2006). It solves the transfer equation in the form

$$dI/d\tau = I - S, \quad (12)$$

where $d\tau = -\kappa\rho dl$ is the differential of the optical depth along a given ray and l is a coordinate along the ray.

The code is parallelized by splitting the calculation into two local parts that are compute-intensive and one that is non-local and fast, so it does not require any computation. Since S is assumed independent of I (scattering is ignored), we can write the solution of Equation (12) as an integral for $I(\tau)$, which is thus split into two parts,

$$I(\tau) = - \underbrace{\int_0^{\tau_0} e^{\tau'-\tau} S(\tau') d\tau'}_{I_{\text{extr}}} - \underbrace{\int_{\tau_0}^{\tau} e^{\tau'-\tau} S(\tau') d\tau'}_{I_{\text{intr}}}, \quad (13)$$

where the subscripts ‘extr’ and ‘intr’ indicate respectively an extrinsic, non-local contribution and an intrinsic, local one. In the first step, we calculate $I_{\text{intr}}(\tau)$, which can be evaluated immediately on all processors in parallel, while the first integral is written in the form $I_{\text{extr}}(\tau) = I_0 e^{\tau_0-\tau}$, where I_0 and τ_0 are already being computed as part of the I_{intr} calculation on neighboring processors and the results included in the last step of the computation.

In the second step, the values of $\tau_0 = \tau$ and $I_0 = I(\tau_0)$ are communicated from the end point of each ray on the previous processor, which cannot be done in parallel, but this does not require any computational time. In the final step one computes

$$I_{\text{extr}}(\tau) = I_0 e^{\tau_0-\tau} \quad (14)$$

and constructs the final intensity as $I(\tau) = -I_{\text{extr}}(\tau) - I_{\text{intr}}(\tau)$.

Instead of solving the radiative transfer equation directly for the intensity, the contribution to the cooling rate $Q(\tau) = I(\tau) - S(\tau)$ is calculated instead, as was done also by Nordlund (1982). This avoids round-off errors in the optically thick part. For further details regarding the implementation we refer to Heinemann et al. (2006). To avoid interpolation, the rays are chosen such that they go through mesh points. The angular integration in Equation (4) is discretized as

$$\nabla \cdot \mathbf{F}_{\text{rad}} = -\frac{4\pi\kappa\rho}{N} \frac{D}{3} \sum_{i=1}^N [I(\mathbf{x}, t, \hat{\mathbf{n}}_i) - S], \quad (15)$$

where i enumerates the N rays with directions $\hat{\mathbf{n}}_i$ and $D/3$ is a correction factor that is relevant when the number of dimensions, D , of the calculation is less than three. It does not affect the steady state, but it affects the cooling rate both in the optically thick and thin regimes; see Appendix A for details. In one dimension with $D = 1$, we have $N = 2$ rays, which are $\hat{\mathbf{n}}_{1,2} = (0, 0, \pm 1)$, while for $D = 2$ we can either have $N = 4$ with $\hat{\mathbf{n}}_{1,2} = (\pm 1, 0, 0)$ and $\hat{\mathbf{n}}_{3,4} = (0, 0, \pm 1)$, or $N = 8$ with the additional 4 combinations $\hat{\mathbf{n}}_{5,\dots,8} = (\pm 1, 0, \pm 1)/\sqrt{2}$. In three dimensions, the correction factor is $D/3 = 1$, so the angular integral is just 4π times the average of the intensity over all directions.

Table 1. Summary of used a and b .

Set	a	b	n	Schwarzschild
A	1	-3.5	3.25	stable
B	1	0	1.5	marginally stable
C	1	1	1	unstable
D	1	5	-1	ultra unstable
E	-1	3	0/0	undefined

Notes. Combinations of exponents a and b and the resulting polytropic index n used in the present study. The characterization with respect to the Schwarzschild stability criterion is based on $\gamma = 5/3$, corresponding to a marginal polytropic index of $n = 1/(\gamma - 1) = 3/2$. Each parameter combination is denoted by a letter A–E, which corresponds later to different sets of runs.

2.5. Parameters and initial conditions

In the following, we measure length in Mm, speed in km s^{-1} , density in g cm^{-3} , and temperature in K. This implies that time, for example, is measured in ks (=1000 s). For the gravitational acceleration, we take $\mathbf{g} = (0, 0, -g)$ with $g = 274 \text{ Mm}^{-1} \text{ km}^2 \text{ s}^{-2}$ being the solar surface value (Stix, 2002). Instead of prescribing T_0 , we prescribe the sound speed c_s , where $c_s^2 = \gamma \mathcal{R}T/\mu$, and fix $c_s = c_{s0} = 30 \text{ km s}^{-1}$ at $z_{\text{bot}} = 0$. With $\mathcal{R} = 8.314 \cdot 10^7 \text{ erg K}^{-1} \text{ mol}^{-1}$ and $\mu = 0.6 \text{ g mol}^{-1}$, this choice corresponds to $T_0 = 38,968 \text{ K}$. We found it instructive to start with an isothermal solution that is in hydrostatic equilibrium, but not in thermal equilibrium, so the upper parts will gradually cool until a static solution is reached. Thus, we use $\rho = \rho_0 \exp(-z/H_p)$, where $H_p = \mathcal{R}T/\mu g$ is the pressure scale height, and ρ_0 is a constant that we set to $\rho_0 = 4 \cdot 10^{-4} \text{ g cm}^{-3}$. This value was chosen based on values from a solar model at a depth of approximately 7 Mm below the surface. However, this particular choice is quite uncritical and just corresponds to renormalizing the opacity. In other words, instead of making a calculation with a ten times larger value of ρ , we can just use an otherwise equivalent calculation with a ten times larger value of κ .

2.6. Simulation strategy

We choose the exponents a and b such that they correspond to five different values of n . In the case $a = -1$, $b = 3$, we have $K(\rho, T) = \text{const}$, but the value of n is undefined. Our choice of parameters is summarized in Table 1. It is convenient to express κ in the form

$$\kappa = \tilde{\kappa}_0 \left(\frac{\rho}{\rho_0} \right)^a \left(\frac{T}{T_0} \right)^b, \quad (16)$$

where $\tilde{\kappa}_0$ is a rescaled opacity and is related to κ_0 by $\tilde{\kappa}_0 = \kappa_0 \rho_0^a T_0^b$. With this choice, the units of $\tilde{\kappa}_0$ are independent of a and b , and always $\text{Mm}^{-1} \text{ cm}^3 \text{ g}^{-1}$ ($= 10^{-8} \text{ cm}^2 \text{ g}^{-1}$). For each value of n , we choose 4 different values of $\tilde{\kappa}_0 = 10^4, 10^5, 10^6$, and $10^7 \text{ Mm}^{-1} \text{ cm}^3 \text{ g}^{-1}$. We note that the actual Kramers opacity for free-free and bound-free transitions with $a = 1$ and $b = -7/2$ has $\kappa_0 = 4.5 \cdot 10^{24} \text{ cm}^5 \text{ g}^{-2}$. This corresponds to $\tilde{\kappa}_0 = 1.54 \cdot 10^{13} \text{ Mm}^{-1} \text{ cm}^3 \text{ g}^{-1}$, which is still six orders of magnitude larger than the largest value we consider in this paper.

¹ <http://pencil-code.googlecode.com/>

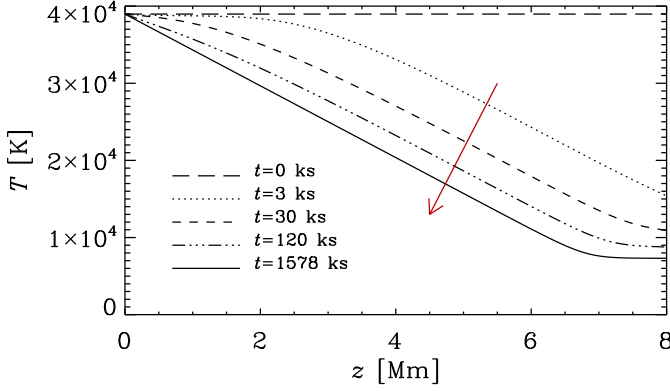


Fig. 1. Vertical temperature profile at five different times $t = 0, 3, 30, 120$, and 1578 ks for Run A6 with $\tilde{\kappa}_0 = 10^6 \text{ Mm}^{-1} \text{ cm}^3 \text{ g}^{-1}$. The arrow represents the direction of the time evolution of the temperature profile.

3. Results

We perform one-dimensional simulations with a resolution of 512 grid points using five sets of values for the exponents a and b in the expression for the Kramers opacity; see Equation (16). Each set of runs is denoted by a letter A–E. In the first four sets of runs, we keep $a = 1$ and change the value of b from $-7/2$, to 0, 1, and 5. For each of these sets, we perform four runs that differ only in the values of $\tilde{\kappa}_0$. The numeral on the label of each run refers to a different value of $\tilde{\kappa}_0$. In Set A, we use $a = 1$ and $b = -7/2$. Runs A4, A5, A6 and A7 correspond to $\tilde{\kappa}_0$ equal to $10^4, 10^5, 10^6$ and $10^7 \text{ Mm}^{-1} \text{ cm}^3 \text{ g}^{-1}$, respectively. All the other designations follow the same scheme. All runs have been started with the same initial isothermal condition. However, the size of the domain changes so as to accommodate the upper isothermal part by a good margin. If the domain is too big, one needs a large number of meshpoints to resolve the resulting strong stratification, and if it is too small, the solution changes in the top part, as will be discussed in Section 3.9.

After a sufficient amount of running time, a unique equilibrium state is reached and the resulting profiles of temperature, density and entropy have a nearly polytropic stratification in the lower part of the domain and a nearly isothermal stratification in the upper part of the domain. An exception are the runs of Set E where the polytropic index is undefined ($n = 0/0$). This will be discussed in more detail in Section 3.8. We summarize the important quantities obtained from all runs in Table 2. These quantities are calculated in the equilibrium state. All runs show a similar evolution of density, temperature and entropy. In the next sections we describe the resulting profiles in more detail.

3.1. Approach toward the final state

As mentioned above, we find it convenient to obtain equilibrium solutions by starting from an isothermal state. The upper layers begin to cool fastest, and eventually a new equilibrium state is reached. We plot the evolution of the temperature profile of Run A6 in Figure 1 as an exemplary case with $\tilde{\kappa}_0 = 10^6 \text{ Mm}^{-1} \text{ cm}^3 \text{ g}^{-1}$. The temperature starts decreasing close to the top boundary, where the radiation is acting as an efficient cooling process. Already after a short time of $t = 3$ ks (1 hours), the temperature has decreased by more than half its

initial value at the top and follows a polytropic solution in most of the domain, where the temperature gradient has a similar value than in the equilibrium state. At $t = 30$ ks (9 hours), close to the upper boundary, an isothermal part is seen to appear. However, it takes more than $t = 1500$ ks (18 days) until the equilibrium solution is reached with a prominent isothermal part of $T \approx 7000$ K. The thermal adjustment time required for reaching the final state will be discussed Section 3.7.

3.2. Temperature stratification

For all runs, the initial isothermal temperature stratification does not stay isothermal. During the simulation the temperature cools down, starting at the upper boundary, near the location where $\tau(z) \approx 1$, which is where the cooling is most efficient. Here,

$$\tau(z) = \int_z^{z_{\text{top}}} \kappa(z') \rho(z') dz' \quad (17)$$

is the optical depth with respect to the surface of the domain. After a certain time the temperature reaches an equilibrium state. The temperature profile can be divided into two distinguishable parts, a nearly polytropic part which starts from the bottom of the domain and extends to a certain height, and a nearly isothermal part which starts from this height and extends to the top of the domain. The transition of the temperature from the initial state to the equilibrium state follows a specific pattern, which is the same for all the runs. The higher the value of $\tilde{\kappa}_0$, the lower the temperature is in the isothermal part and the longer it takes to reach this state. Increasing the normalized opacity $\tilde{\kappa}_0$ by three orders of magnitude results in a factor of five for Set A and a factor of three for Set D. As the exponent b changes from the smallest value in Set A to the largest one in Set D, the slope of the temperature decreases with height. This means that the polytropic part of the atmosphere is smaller for larger values of b . Note that the size of the domain is chosen larger for smaller values of b . For Sets A, B and C, the temperature in the polytropic part is almost the same for different values of $\tilde{\kappa}_0$, although for the lowest value of $\tilde{\kappa}_0$ the temperature deviates somewhat. However, in Set D, for different values of $\tilde{\kappa}_0$, the slope of the temperature is different for each value of $\tilde{\kappa}_0$. This has to do with the fact that in this case with $(b - 3)/(1 + a) = -1$ the stratification is no longer a polytropic one. (A polytrope with $n = -1$ would have constant pressure, which is unphysical.)

The temperatures in the isothermal part also show a dependency on b . For $\tilde{\kappa}_0 = 10^4 \text{ Mm}^{-1} \text{ cm}^3 \text{ g}^{-1}$ the temperature in Run A4 is $T \approx 2.2 \cdot 10^4$ K, whereas in Run D4 the value is $T \approx 2.9 \cdot 10^4$ K. A similar behavior can also be seen for the other values of $\tilde{\kappa}_0$. Next, we calculate the optical depth for all runs. We find that the transition point from the polytropic part to the isothermal part coincides with the $\tau \approx 1$ surface. We indicate the surface $\tau \approx 1$ by dots in all plots in Figure 2. The polytropic part corresponds to the optically thick part with $\tau > 1$ and the isothermal part corresponds to the optically thin part with $\tau < 1$. For each set, the transition point depends on the value of $\tilde{\kappa}_0$. As we go from smaller to larger values of $\tilde{\kappa}_0$, the surface shifts to larger heights and becomes cooler. This is due to the fact that the radiative heat conductivity K has an inverse relation with $\tilde{\kappa}_0$ and is directly proportional to the flux. Therefore, by increasing the value of $\tilde{\kappa}_0$, K decreases and, as a consequence, the radiative flux also decreases. By decreasing the flux, the effective temperature decreases as $T_{\text{eff}} \propto F_{\text{rad}}^{1/4}$. This means that the temperature at the surface is smaller for larger values of $\tilde{\kappa}_0$. The $\tau \approx 1$ surfaces lie for Set A on the polytropic part of the temperature

Table 2. Summary of the runs.

Run	a	b	n	$\tilde{\kappa}_0$	z_{top}	$z_{\tau=1}$	$\rho_{\tau=1}$	τ_{adjust}	T_{eff}	K_{bot}
A4	1	-3.5	3.25	10^4	8	2.8	$1.0 \cdot 10^{-4}$	50	23600	$3.9 \cdot 10^{-6}$
A5	1	-3.5	3.25	10^5	8	5.2	$1.7 \cdot 10^{-5}$	90	13900	$4.6 \cdot 10^{-7}$
A6	1	-3.5	3.25	10^6	8	6.6	$2.5 \cdot 10^{-6}$	700	7800	$4.6 \cdot 10^{-8}$
A7	1	-3.5	3.25	10^7	8	7.4	$3.7 \cdot 10^{-7}$	15000	4400	$4.4 \cdot 10^{-9}$
B4	1	0	1.5	10^4	5	1.4	$2.2 \cdot 10^{-4}$	40	26600	$4.53 \cdot 10^{-6}$
B5	1	0	1.5	10^5	5	2.9	$9.0 \cdot 10^{-5}$	60	16300	$5.15 \cdot 10^{-7}$
B6	1	0	1.5	10^6	5	3.8	$3.7 \cdot 10^{-5}$	400	9300	$5.38 \cdot 10^{-8}$
B7	1	0	1.5	10^7	5	4.3	$1.6 \cdot 10^{-5}$	5000	5200	$5.08 \cdot 10^{-9}$
C4	1	1	1	10^4	4	1	$2.6 \cdot 10^{-4}$	7	27600	$5.1 \cdot 10^{-6}$
C5	1	1	1	10^5	4	2.3	$1.3 \cdot 10^{-4}$	20	17400	$5.6 \cdot 10^{-7}$
C6	1	1	1	10^6	4	3.1	$7.0 \cdot 10^{-5}$	200	10100	$6.0 \cdot 10^{-8}$
C7	1	1	1	10^7	4	3.4	$3.9 \cdot 10^{-5}$	2100	5700	$6.1 \cdot 10^{-9}$
D4	1	5	-1	10^4	2	0.2	$3.6 \cdot 10^{-4}$	6	31000	$1.1 \cdot 10^{-5}$
D5	1	5	-1	10^5	2	0.8	$2.8 \cdot 10^{-4}$	7	23100	$1.3 \cdot 10^{-6}$
D6	1	5	-1	10^6	2	1	$2.8 \cdot 10^{-4}$	80	15600	$1.9 \cdot 10^{-7}$
D7	1	5	-1	10^7	2	1	$3.2 \cdot 10^{-4}$	700	10100	$3.1 \cdot 10^{-8}$
E4	-1	3	0/0	10^4	4	3.0	$8.7 \cdot 10^{-5}$	6	23700	$4.47 \cdot 10^{-6}$
E5	-1	3	0/0	10^5	4	3.6	$5.6 \cdot 10^{-5}$	45	14900	$4.47 \cdot 10^{-7}$
E6	-1	3	0/0	10^6	4	3.8	$3.9 \cdot 10^{-5}$	400	8800	$4.47 \cdot 10^{-8}$

Notes. In the table, the size of the domain z_{top} in units of Mm, the density at the surface $\rho_{\tau=1}$ in units of g cm^{-3} , the height of the surface $z_{\tau=1}$ in Mm, the thermal adjustment time τ_{adjust} in ks, the effective temperature T_{eff} in K, radiative heat conductivity at the bottom of the domain K_{bot} in $\text{g cm}^{-3} \text{K}^{-1} \text{Mm}^{-1} \text{km}^3 \text{s}^{-3}$ and the normalized opacity $\tilde{\kappa}_0 = \kappa_0 \rho_0^a T_0^b$ in units of $\text{Mm}^{-1} \text{cm}^3 \text{g}^{-1}$ are shown for each run. The second to the sixth columns show quantities which are input parameters to the models whereas the quantities in last five columns are the results of the simulations, computed from the equilibrium state.

profile. However, by increasing the value of b , the location of the surfaces shift along the polytropic part of the temperature profile.

3.3. Entropy stratification

We plot the entropy profiles for all sets of runs in the equilibrium state in the last column of Figure 2. For Runs C6–7 and D4–8, the entropy decreases in the polytropic part and starts to increase in the isothermal part. All runs show a positive vertical entropy gradient in the isothermal part. In the lower part, for Set A, the entropy gradient is positive, $\nabla_z s > 0$, while for Set B it is constant and equal to zero, $\nabla_z s \approx 0$. This shows that for Set B, the atmospheres are isentropic. In Sets C and D, except for the case $\tilde{\kappa}_0 = 10^4 \text{ Mm}^{-1} \text{cm}^3 \text{g}^{-1}$, the entropy gradient is negative, $\nabla_z s < 0$. This means that their atmospheres are convectively unstable. (Convection will of course not occur in our one-dimensional model, but we will obtain the so-called hydrostatic reference solution that is used to compute the Rayleigh number, as will also be done later in this paper.) In Set D the entropy gradients are larger than in case C where their atmospheres are marginally unstable. In the isothermal part of Set C, the entropy gradient is much larger than in Set D. For each set of runs, as we go from smaller values of $\tilde{\kappa}_0$ to larger ones, the entropy profiles have larger gradients.

3.4. Incoming and outgoing intensity profiles

It is instructive to inspect the vertical profiles of the intensity for rays pointing in the up- and downward directions, $\hat{n} = (0, 0, \pm 1)$, denoted in the following by I^\pm . If we have just these two rays, the energy flux is given by $F_{\text{rad}} = (2\pi/3)(I^+ - I^-)$.

In thermal equilibrium, the difference between I^+ and I^- must be constant. This is indeed the case; see Figure 3, where we plot I^+ and I^- and compare with S . The vertical lines in this figure represents the difference between I^+ and I^- , where $I^+ - I^- \approx 10^4 \text{ erg cm}^2 \text{s}^{-1}$ in the whole domain as we have radiative equilibrium $\nabla \cdot \mathbf{F}_{\text{rad}} = 0$. Radiative equilibrium also demands that $J = S$, so S has to be equal to the average of I^+ and I^- , which is indeed the case.

3.5. Radiative heat conductivity

In Sets A, B, and C, the value of radiative heat conductivity K turns out to be constant in the optically thick part of the atmosphere, but not for Set D. The value of K at the bottom of the optically thick part of the domain is denoted in Table 2 by K_{bot} , and agrees roughly with

$$K_{\text{bot}} \approx K_0 \equiv \frac{16\sigma_{\text{SB}}T_0^3}{3\tilde{\kappa}_0\rho_0}. \quad (18)$$

Indeed, it has almost the same order of magnitude for A, B and C, independently of the value of b , but it is one order of magnitude larger for Set D. This is due to the fact that in this set the density is lower in the optically thick part compared to the other sets. Moreover, as we go from higher values of $\tilde{\kappa}_0$ to the lower ones, the radiative heat conductivity increases. This can be explained by the inverse proportionality of K with opacity as $K \propto 1/\tilde{\kappa}_0$. For smaller values of $\tilde{\kappa}_0$, K is larger and vice versa. As an example, we plot in Figure 4 the resulting vertical profiles of radiative heat conductivity for Set C. As we can see, K is constant in the optically thick part and starts to increase in the optically thin part. In the optically thin part, $\kappa\rho$ decreases, so K increases as $K \propto 1/\kappa$. To maintain $\nabla \cdot \mathbf{F}_{\text{rad}} = 0$, the

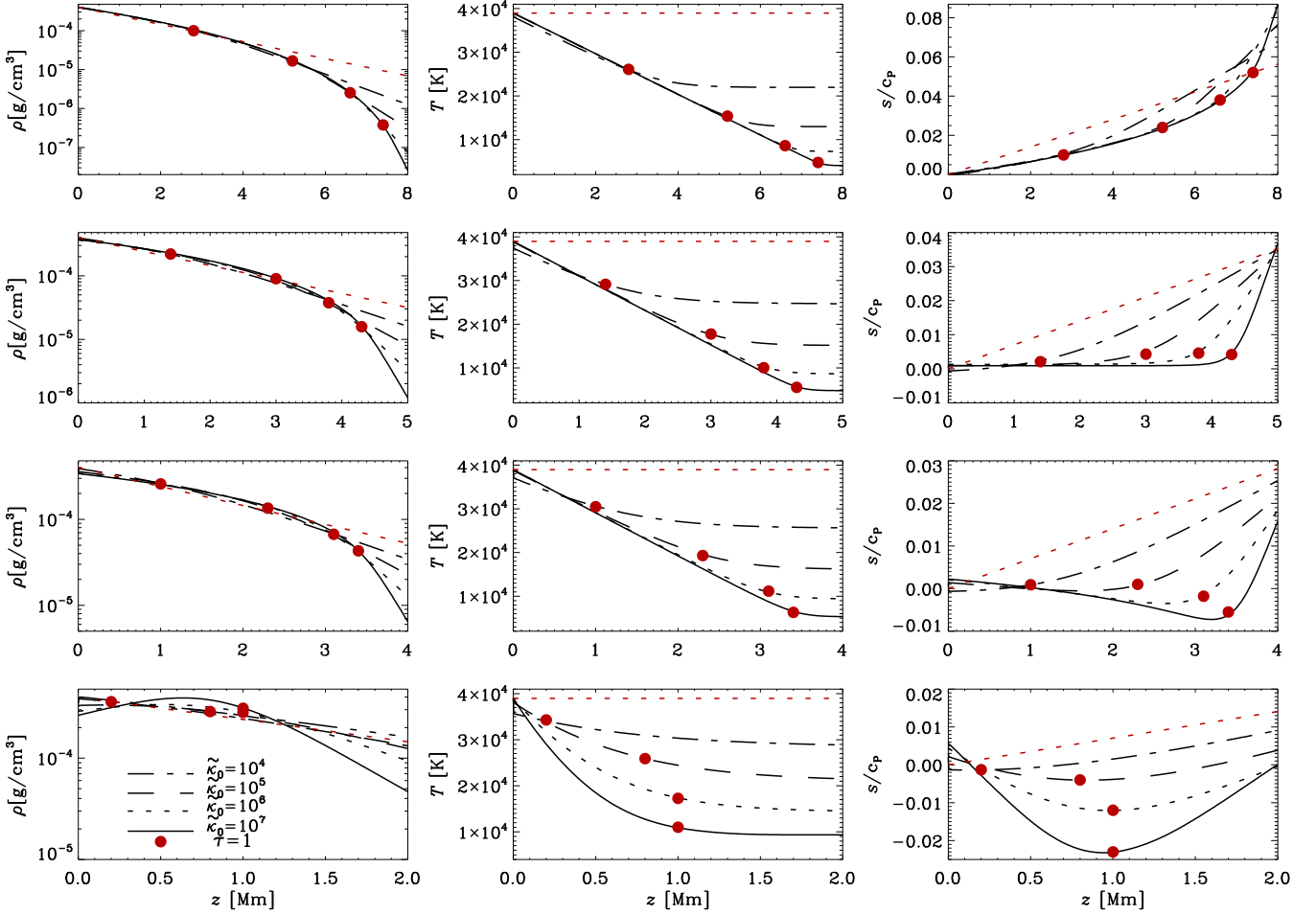


Fig. 2. Density, temperature and entropy of the equilibrium state versus height, from left to right, for Sets A, B, C and D, from top to bottom. The four different lines in each plot corresponds to the value of the rescaled opacity $\tilde{\kappa}_0 = 10^4, 10^5, 10^6, 10^7 \text{ Mm}^{-1} \text{ cm}^3 \text{ g}^{-1}$. The dots in all plots represent the surface $\tau \approx 1$. The red dotted lines represent the initial profile of each set.

modulus of ∇T has to decrease. As K increases even further, a thermostatic equilibrium can be satisfied if ∇T comes close to zero.

3.6. Effective temperature

The effective temperature T_{eff} of all runs is calculated from the radiative flux F_{rad} ,

$$T_{\text{eff}} = \left(\frac{F_{\text{rad}}}{\sigma_{\text{SB}}} \right)^{1/4}. \quad (19)$$

The values of T_{eff} of all sets of runs are summarized in Table 2. By increasing the value of b , T_{eff} also increases. The value of T_{eff} decreases as we go from lower to higher opacities for each set. We plot T_{eff} versus $\tilde{\kappa}_0$ in Figure 5 for Sets A, C and D where the values of T_{eff} are represented by crosses, circles and stars, respectively. For each set of runs, we fit a line to T_{eff} versus $\tilde{\kappa}_0$. We find that T_{eff} has a power law relation with $\tilde{\kappa}_0$. The power of $\tilde{\kappa}_0$, which is the slope of the plot, depends on the polytropic index and therefore on b . For larger values of b , the power is smaller than for smaller values of b . Additionally, the offset shows also a weak dependence on b . A power law relation between T_{eff} and the opacity of roughly $1/4$ can be expected, because of the linear relation of the radiative flux and the opacity. Toward larger

b , this dependency is no longer accurate. We also calculate for each run the corresponding optical depth where $T = T_{\text{eff}}$. For all runs, T_{eff} corresponds to the optical depth $\tau \approx 1/3$. This is less than what is expected for a gray atmosphere, where $T_{\text{eff}} = T$ at $\tau \approx 2/3$. This is presumably because our integration of τ we have not concluded the contribution between ∞ and $z = z_{\text{top}}$.

3.7. Thermal adjustment time

In our simulations we define a thermal adjustment time τ_{adjust} as the time it takes for each run to reach its final isothermal equilibrium temperature to within 1%. The unit of τ_{adjust} is ks (cf. Section 2.5). The value of τ_{adjust} for all runs is summarized in Table 2. As we can see in Table 2, the thermal adjustment time becomes smaller for larger b and smaller n . For each set of runs, τ_{adjust} grows approximately linearly with $\tilde{\kappa}_0$, although for $\tilde{\kappa}_0 \lesssim 10^5$, the dependency is more shallow. For larger values of $\tilde{\kappa}_0$, τ_{adjust} seems to have a stronger dependency on b . We speculate that the reason for increasing the value of τ_{adjust} for higher values of $\tilde{\kappa}_0$ is that by increasing the opacity the energy transport via radiation becomes less efficient as the mean free path of the photon decreases. But it seems that there exists a threshold of efficiency, leading to a larger adjustment time for the lowest values of $\tilde{\kappa}_0$, as expected. We plot the vertical dependence of the

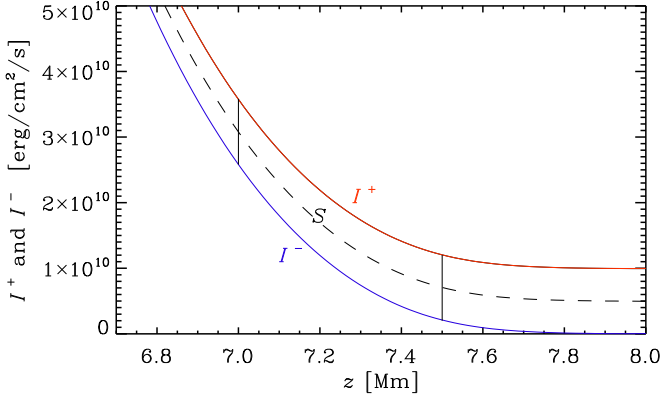


Fig. 3. Source function and vertical profiles of incoming and outgoing intensity near the surface for Run A7. The dashed line represents the source function and the solid lines represent the incoming intensity I^+ (red) and outgoing intensity I^- (blue), respectively. The vertical lines represent the (constant) difference between I^+ and I^- .

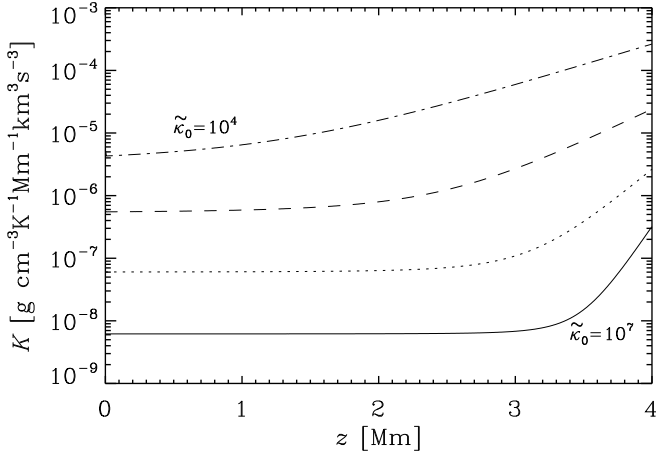


Fig. 4. Radiative heat conductivity K versus height for Set C. K is plotted for different values of $\tilde{\kappa}_0$ where $\tilde{\kappa}_0 = 10^4 \text{ Mm}^{-1} \text{ cm}^3 \text{ g}^{-1}$ is shown by dotted-dashed line, $\tilde{\kappa}_0 = 10^5 \text{ Mm}^{-1} \text{ cm}^3 \text{ g}^{-1}$ dashed line, $\tilde{\kappa}_0 = 10^6 \text{ Mm}^{-1} \text{ cm}^3 \text{ g}^{-1}$ dotted line and $\tilde{\kappa}_0 = 10^7 \text{ Mm}^{-1} \text{ cm}^3 \text{ g}^{-1}$ solid line.

mean free path of the photons $\ell = 1/\kappa\rho$ normalized by the size of the domain L for Set C.

As we can see in Figure 6, the mean free path increases over several orders of magnitude from the bottom of the domain to the top. Furthermore, ℓ is larger for smaller $\tilde{\kappa}_0$. In the optically thick part, the difference in ℓ is one order of magnitude, which is equal to a corresponding change in $\tilde{\kappa}_0$. In the optically thin part, the difference of the values of ℓ becomes smaller, as we reach the top of the domain. For $\tilde{\kappa}_0 = 10^7 \text{ Mm}^{-1} \text{ cm}^3 \text{ g}^{-1}$, ℓ is the smallest and three orders of magnitude smaller than for $\tilde{\kappa}_0 = 10^4 \text{ Mm}^{-1} \text{ cm}^3 \text{ g}^{-1}$. Furthermore, ℓ is 10 times the size of the domain for $\tilde{\kappa}_0 = 10^4 \text{ Mm}^{-1} \text{ cm}^3 \text{ g}^{-1}$, which makes the cooling more efficient. We would have expected to see a large change in the mean free path as we go through the surface. Nevertheless, the exponential growth seems to be roughly the same throughout the domain, at least for the smallest value of $\tilde{\kappa}_0$.

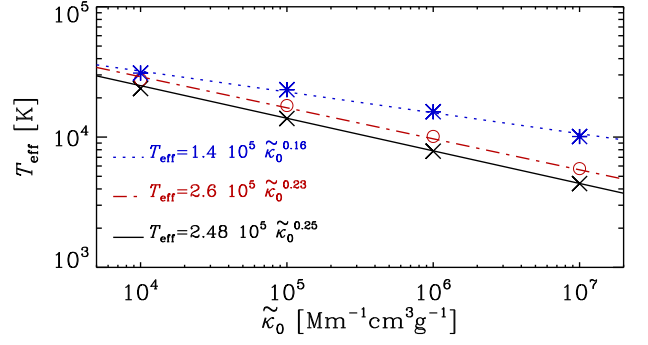


Fig. 5. Vertical profile of effective temperature T_{eff} for three different Sets A, C, and D. The crosses, circles and stars show the values of T_{eff} for different values of $\tilde{\kappa}_0$ for Sets A, C, and D, respectively. Different lines correspond to line fit of T_{eff} with normalized opacity $\tilde{\kappa}_0$.

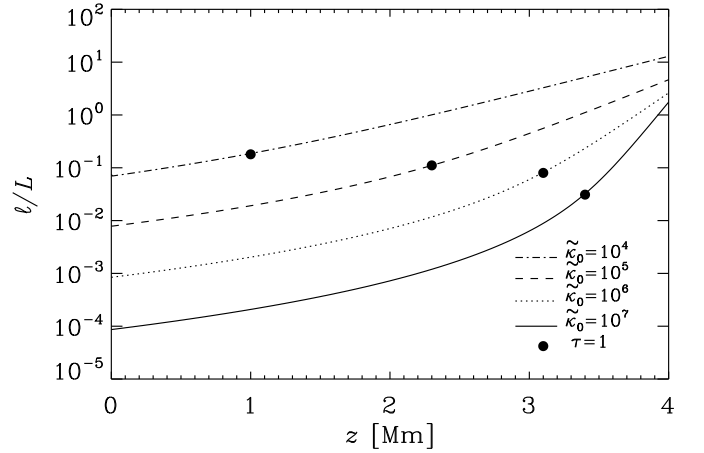


Fig. 6. Normalized mean free path of photons ℓ/L versus height for Set C. The dots represent the surface $\tau \approx 1$.

3.8. Properties of an atmosphere with undefined n

By choosing $a = -1$ and $b = 3$, we have a constant heat conductivity K that is independent of density and temperature as the heat conductivity is given by Equation (18). The value of n is given by

$$n = \frac{3-3}{1-1} = \frac{0}{0}. \quad (20)$$

In this case, we expect to have only a polytropic solution which satisfies the thermostatic equilibrium if $\nabla_z T = \text{const}$, but it is then unclear how ρ varies. We plot in Figure 7 the profiles of temperature, density, and entropy for all the runs of Set E. As expected, there is no isothermal part. The slope of temperature decreases approximately linearly as we go to higher values of $\tilde{\kappa}_0$, because K is related to the normalized opacity as $1/\tilde{\kappa}_0$. Although, we do not get any solution that has a transition from the polytropic part to the isothermal part, the atmosphere has a surface where $\tau = 1$ and it is shown with red dots in all panels of Figure 7. In contrast to the other sets, A, B, C, and D, the temperature profiles look qualitatively different. As in Sets A, B, and C, in the optically thick part, the different temperature profiles have nearly the same gradient, while in Set E, the gradient differ for different values of $\tilde{\kappa}_0$. This is due to the fact that the

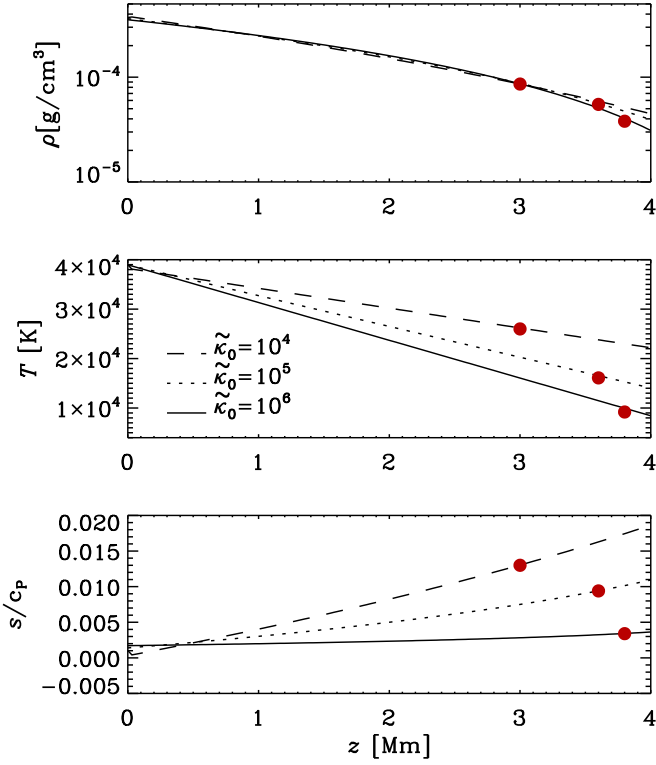


Fig. 7. Temperature, density and entropy profiles for $n = 0/0$ and three values of $\kappa_0 = 10^4, 10^5$, and $10^6 \text{ Mm}^{-1} \text{ cm}^3 \text{ g}^{-1}$ for Set E in the equilibrium state. The red dots present the surface of the model where $\tau = 1$.

thermostatic equilibrium should be obeyed with the same constant K . In the second panel of Figure 7, the density profiles are almost the same for different values of κ_0 in the optically thick part and they decrease in the optically thin part. The density for higher values of κ_0 drops faster than in the case of smaller κ_0 . In all cases, K is constant in both optically thick and thin parts, but an interesting aspect is that its bottom value K_{bot} is of the same order of magnitude as in Sets A, B, and C. In the third panel of Figure 7, we plot entropy profiles for the different values of κ_0 . In all cases the entropy increases with a constant slope, which depends on κ_0 . By plotting a versus b for different values of the polytropic index n , we see that all lines, which corresponds to different values of n intersect each other at $K = K_0 = \text{const}$; see Figure 8. This means that the solution for constant K can belong to any of these polytropic indexes.

In the absence of convection, all the energy is carried by radiation and we have $\nabla = \nabla_{\text{rad}}$. We calculate the value of the polytropic index n using the superadiabatic gradient, which is given by $\Delta \nabla = \nabla - \nabla_{\text{ad}} = c_p^{-1} ds/d \ln p$, where

$$\nabla_{\text{ad}} = 1 - \frac{1}{\gamma} \quad (21)$$

is the adiabatic double-logarithmic temperature gradient. We calculate the value of the polytropic index n using for an isothermal gas as $n = d \ln \rho / d \ln T = d \ln p / d \ln T - 1 = \nabla^{-1} - 1$ and write $\Delta \nabla$ in terms of ∇ . Interestingly, for $a = -1$ and $b = 3$, in which case n is undefined, the solution turns out to be close to $3/2$, which would be an isentropic radiative atmosphere. As we see, this is actually not quite the case as we see in the last panel of Figure 7, but the values of s are small.

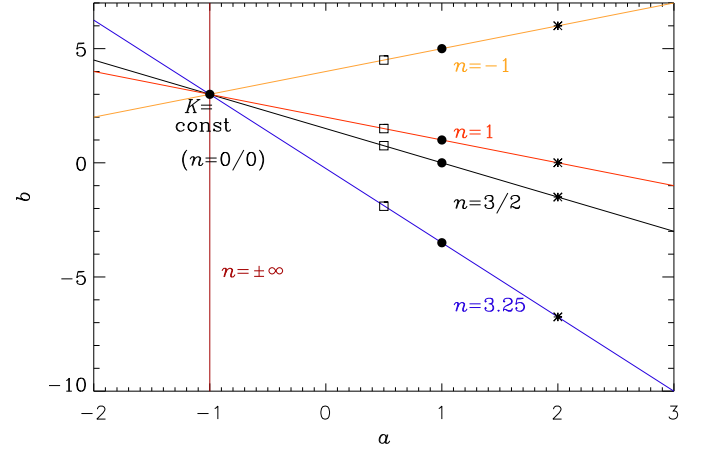


Fig. 8. b versus a for different values of the polytropic index n . The black dots represents the combination of $a = 1$ with different values of b which are used in the main simulation; see Table 2. The stars represent the combination of $a = 2$ and squares represent $a = 0.5$ with different values of b ; see Table 3.

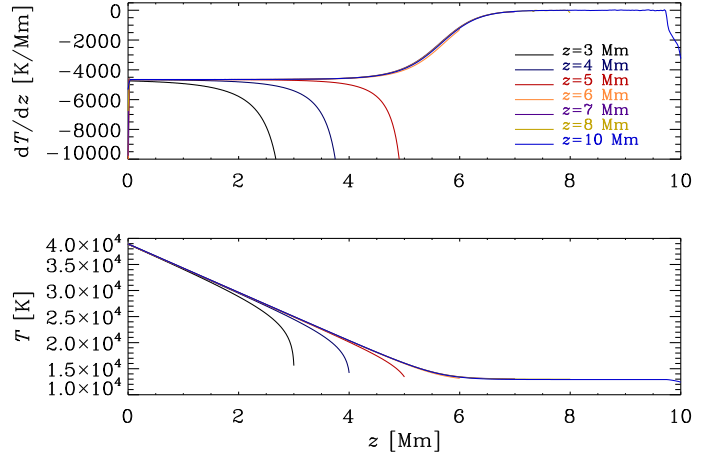


Fig. 9. Gradient temperature (upper panel) and temperature profile (lower panel) of seven different sizes of the domain $z = 3, 4, 5, 6, 7, 8$, and 10 Mm of Run A5.

3.9. Dependence on the size of the domain

In our model, the size of the domain plays an important role in getting the polytropic and isothermal solutions for the temperature profile. The domain has to be big enough so that the transition point lies inside the domain. In Figure 9, we show the vertical dependence of temperature for six domain sizes for Run A5. If the size of the domain is $z < 7 \text{ Mm}$, it is too small to obtain the isothermal part where $\nabla_z T = 0$ and a boundary layer is produced. The opacity is then too large to let the heat be radiated away. A size of around $z = 8 \text{ Mm}$ is sufficient to get the isothermal part. However, a domain size that is too large ($z = 10 \text{ Mm}$) leads to numerical difficulties near the top boundary, if the resolution is too low. For all the runs shown in Table 2, we have always started by performing several test simulations to find a suitable domain size.

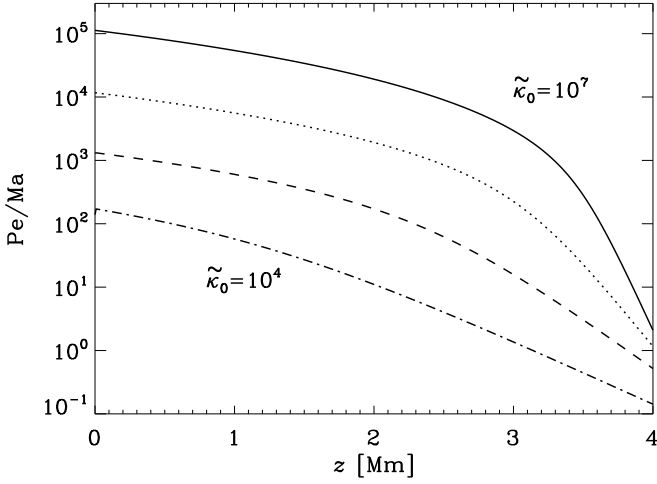


Fig. 10. $\widetilde{\text{Pe}}$ versus z for Set C using different values of $\tilde{\kappa}_0$: $\tilde{\kappa}_0 = 10^4 \text{ Mm}^{-1} \text{ cm}^3 \text{ g}^{-1}$ (dotted-dashed line), $\tilde{\kappa}_0 = 10^5 \text{ Mm}^{-1} \text{ cm}^3 \text{ g}^{-1}$ (dashed line), $\tilde{\kappa}_0 = 10^6 \text{ Mm}^{-1} \text{ cm}^3 \text{ g}^{-1}$ (dotted line) and $\tilde{\kappa}_0 = 10^7 \text{ Mm}^{-1} \text{ cm}^3 \text{ g}^{-1}$ (solid line).

3.10. Radiative diffusivity

In numerical simulations, the radiative diffusivity χ is an important parameter, and has the same dimension as the kinematic viscosity ν . Both χ and ν determine whether the results of numerical turbulence simulations are reliable or not and whether they are able to dissipate all the energy within the mesh. In a numerical simulation we are restricted to a certain number of grid points. If the diffusion of the temperature in a simulation is very small, it can happen that the changes in the temperature are too large over the distance of neighboring grid points. Hence, the changes of the temperature cannot be resolved in such a simulation. Therefore, it is important to measure how large are the thermal diffusivity in our models of a radiative atmosphere. The Péclet number is a dimensionless number that quantifies the importance of advective and diffusive term, which is here defined as

$$\text{Pe} = u_{\text{rms}} H_p / \chi, \quad (22)$$

where H_p is a pressure scale height and u_{rms} is rms velocity. The radiative diffusivity is defined as

$$\chi = K / c_p \rho, \quad (23)$$

where K is evaluated using Equation (7). As we do not solve for a velocity equation in our model, so we use instead the sound speed, which can be related to u_{rms} via the Mach number $\text{Ma} = u_{\text{rms}} / c_s$. The normalized Péclet number in our simulation $\widetilde{\text{Pe}}$ is then given by

$$\widetilde{\text{Pe}} \equiv \text{Pe} / \text{Ma} = c_s H_p / \chi. \quad (24)$$

As an example, we plot $\widetilde{\text{Pe}}$ for Set C in Figure 10. As we can see in Figure 10, $\widetilde{\text{Pe}}$ is a large number for the optically thick part and it decreases as we go toward the optically thin part. This can be explained with Equation (23), where χ is proportional to K . In the optically thin part, K increases, so χ increases. As a result, $\widetilde{\text{Pe}}$ decreases. $\widetilde{\text{Pe}}$ is also larger for the larger value of $\tilde{\kappa}_0$.

Table 3. Summary of the result of different value of a and b with the same polytropic index n .

Run	a	b	n	$z_{\tau=1}$	T_{eff}
F1	0.5	-1.9	3.25	5.3	13900
F2	1	-3.5	3.25	5.2	13900
F3	2	-6.75	3.25	5.1	13400
G1	0.5	0.75	1.5	3.2	16600
G2	1	0	1.5	2.9	16300
G3	2	-1.5	1.5	2.7	16100
H1	0.5	1.5	1	2.6	17100
H2	1	1	1	2.3	17500
H3	2	0	1	2.1	18100
I1	0.5	4.5	-1	1.1	21800
I2	1	5	-1	0.8	23100
I3	2	6	-1	0.6	23700

Notes. $z_{\tau=1}$ is in the units of Mm and represents the position where $\tau \approx 1$ and the effective temperature T_{eff} in units of K. The value of $tkapz$ is the same for all the runs, $tkapz = 10^5 \text{ Mm}^{-1} \text{ cm}^3 \text{ g}^{-1}$.

3.11. The same polytropic index with different a and b

As we can see in Figure 8, for a certain value of the polytropic index, we can choose different combinations of a and b . For each value of n that we have in Table 2, we choose two different other combinations of a and b with the same value of $\tilde{\kappa}_0 = 10^5 \text{ Mm}^{-1} \text{ cm}^3 \text{ g}^{-1}$. For example for the polytropic index $n = 1$ we choose two other combinations as $a = 0.5$ and $b = 1.5$ for one set and $a = 2$ and $b = 0$ for another one (see Table 3). We run eight more simulations with the same initial conditions as in previous runs and we obtain a similar equilibrium solution for the same polytropic index n . We calculate the effective temperature and the position where $\tau \approx 1$ as reference parameters with our old runs. The results are summarized in Table 3. For each set of runs with the same polytropic index, we labeled the runs similarly to those in Table 2.

As we see in Table 3, for each set of runs the effective temperature does not vary strongly, but there is a systematic behavior. By increasing the value of a , the effective temperature increases when $n < 3/2$ and decreases when $n \geq 3/2$, but the surface is shifted to the lower part of the domain for all sets. The stratification of temperature and other important properties of these atmospheres can be explained analogously to those of Sets A, B, C and D. As an example, we plot in Figure 11 the temperature profiles (upper panel) and radiative diffusivity χ (lower panel) for Set H. In the optically thick part, χ is the same for different combinations of a and b for the same n . However, in the optically thin part, χ becomes larger for larger values of a . This can be explained using Equation (23) where the density decreases through the upper part of the domain where $\tau < 1$.

3.12. Optically thick case with radiative boundary

To compare our results with those in the optically thick approximation, we adopt the radiative boundary condition,

$$-K \frac{dT}{dz} = \sigma_{\text{SB}} T^4 \quad \text{on } z = z_{\text{top}}, \quad (25)$$

and keep all other conditions the same as in the radiative transfer calculation, except that $-\nabla \cdot \mathbf{F}_{\text{rad}}$ in Equation (3) is replaced by $K \nabla^2 T$. Here, we have assumed K to be constant,

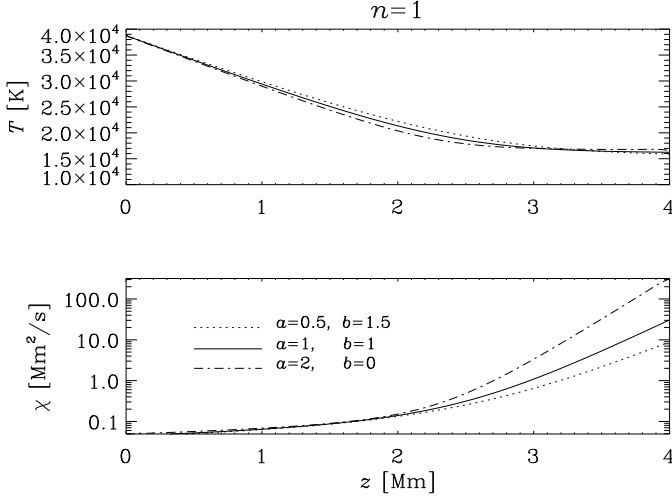


Fig. 11. Profile of T and χ for Set H.

so we shall from now on refer to its value as K_0 , so our solutions will be polytropes with constant polytropic index $n = d \ln \rho / d \ln T$ and constant double-logarithmic temperature gradient $\nabla = d \ln T / d \ln p$.

The value of $\nabla = 1/(1+n)$ can be computed from the equations governing hydrothermal equilibrium,

$$\frac{dp}{dz} = -\rho g, \quad \frac{dT}{dz} = -\frac{F_{\text{rad}}}{K_0}, \quad (26)$$

which yields

$$\nabla = \frac{d \ln T}{d \ln p} = \frac{p}{T \rho} \frac{F_{\text{rad}}}{g K_0} = \nabla_{\text{ad}} c_p \frac{F_{\text{rad}}}{g K_0}. \quad (27)$$

Such a model is characterized by choosing values for n and K_0 . This is analogous to the case with radiative transfer, where n and $\tilde{\kappa}_0$ are specified, and $\tilde{\kappa}_0$ is related to K_0 via Equation (18). Here, it is convenient to define a non-dimensional radiative conductivity as

$$\mathcal{K} = \frac{g K_0}{c_p \sigma_{\text{SB}} T_{\text{bot}}^4} \frac{\nabla}{\nabla_{\text{ad}}}. \quad (28)$$

The radiative flux is then given by

$$F_{\text{rad}} = K_0 \frac{g}{c_p} \frac{\nabla}{\nabla_{\text{ad}}} = \mathcal{K} \sigma_{\text{SB}} T_{\text{bot}}^4, \quad (29)$$

so we get the temperature at the top immediately as

$$T_{\text{top}} = (F_{\text{rad}} / \sigma_{\text{SB}})^{1/4} = \mathcal{K}^{1/4} T_{\text{bot}}. \quad (30)$$

Since the temperatures at top and bottom are now known, the thickness of the layer cannot be chosen independently and is instead given by

$$d = (T_{\text{bot}} - T_{\text{top}}) K_0 / F_{\text{rad}} = \frac{c_p (T_{\text{bot}} - T_{\text{top}})}{g \nabla / \nabla_{\text{ad}}}. \quad (31)$$

Again, this is analogous to the case with radiative transfer, where the thickness of the optically thick layer with nearly constant K emerges as a result of the calculation. In Table 4 we present models for the same parameters as in Table 2. In agreement with our radiative transfer calculations, we have here treated $\tilde{\kappa}_0$ (instead of \mathcal{K}) as our main input parameter (in addition to n). We

have used Equation (18) to convert $\tilde{\kappa}_0$ into K_0 and then used Equation (28) to compute \mathcal{K} . It turns out that there is good agreement regarding the values of d , ρ_{top} , and T_{top} between the optically thick approximation using a radiative upper boundary condition and the radiative transfer calculations. However, unlike Figure 5, the data in Table 4 show power law dependence of T_{eff} versus $\tilde{\kappa}_0$ with the same exponent of $1/4$ in all cases.

Table 4. Summary of model parameters as a function of n and $\tilde{\kappa}_0$ as obtained from the optically thick approximation with radiative upper boundary condition.

n	$\tilde{\kappa}_0$	d	ρ_{top}	T_{top}	ξ	$\rho_{\text{bot}}/\rho_{\text{top}}$
3.25	10^4	3.09	$8.3 \cdot 10^{-5}$	24600	0.40	4.5
3.25	10^5	5.40	$1.3 \cdot 10^{-5}$	13800	0.13	28.9
3.25	10^6	6.70	$2.1 \cdot 10^{-6}$	7800	0.06	187
3.25	10^7	7.44	$3.2 \cdot 10^{-7}$	4400	0.03	1220
1.50	10^4	1.37	$2.2 \cdot 10^{-4}$	28100	1.04	1.6
1.50	10^5	2.93	$8.9 \cdot 10^{-5}$	15800	0.27	3.9
1.50	10^6	3.80	$3.8 \cdot 10^{-5}$	8900	0.12	9.2
1.50	10^7	4.30	$1.6 \cdot 10^{-5}$	5000	0.06	21.8
1.00	10^4	0.94	$2.8 \cdot 10^{-4}$	29700	1.61	1.3
1.00	10^5	2.25	$1.4 \cdot 10^{-4}$	16700	0.38	2.3
1.00	10^6	2.99	$8.0 \cdot 10^{-5}$	9400	0.16	4.1
1.00	10^7	3.41	$4.5 \cdot 10^{-5}$	5300	0.08	7.4

We emphasize that the only place where the choice of density enters our calculation is in Equation (18) when we convert $\tilde{\kappa}_0$ into K_0 . As already indicated at the end of Section 2.5, an increase of ρ_0 by some factor is equivalent to an increase of $\tilde{\kappa}_0$ by the same factor. We recall here that ρ_0 enters both as the initial density at the bottom and in the definition of opacity through Equation (16). The latter ensures that the opacity only changes through changes in $\tilde{\kappa}_0$, and not also through changes in ρ_0 .

3.13. Convection

We now consider two-dimensional convection and compare again results from the optically thick approximation using a radiative upper boundary condition with a calculation using radiative transfer. The control parameter characterizing onset and amplitude of convection is the Rayleigh number,

$$\text{Ra} = \frac{g d^4}{\nu \chi_{\text{mid}}} \left(-\frac{ds}{dz} \right)_{\text{mid}}, \quad (32)$$

where $(-c_p^{-1} ds/dz)_{\text{mid}} = (\nabla - \nabla_{\text{ad}})/H_{\text{p}}^{\text{mid}}$ is the superadiabatic gradient of the unstable, non-convecting hydrostatic reference solution, and $H_{\text{p}}^{\text{mid}} = \nabla_{\text{ad}} c_p T_{\text{mid}}/g$ is the pressure scale height in the middle of the optically thick layer. Furthermore, we define the Prandtl number as $\text{Pr} = \nu/\chi_{\text{mid}}$, where χ_{mid} is the radiative diffusivity in the middle of the optically thick layer. In Table 5 we list the values of the product Pr Ra , as well as d and χ_{mid} for models with $n = 1$ and different values of \mathcal{K} . We adopt periodic boundary condition in the x direction over a domain with side length L_x . When we adopt the diffusion approximation we take $z_{\text{top}} = d$, where d is calculated from Equation (31) and given in Table 5. The mid-layer is then at $z = d/2$, which is also the case when using radiative transfer, where the value of $z_{\text{top}} = d$ is again chosen to be sufficiently large.

It turns out that for $\text{Pr} = 1$, the critical value for the onset of convection is at $\mathcal{K} \gtrsim 0.2$ (corresponding to $\text{Ra} \lesssim 710$) in the op-

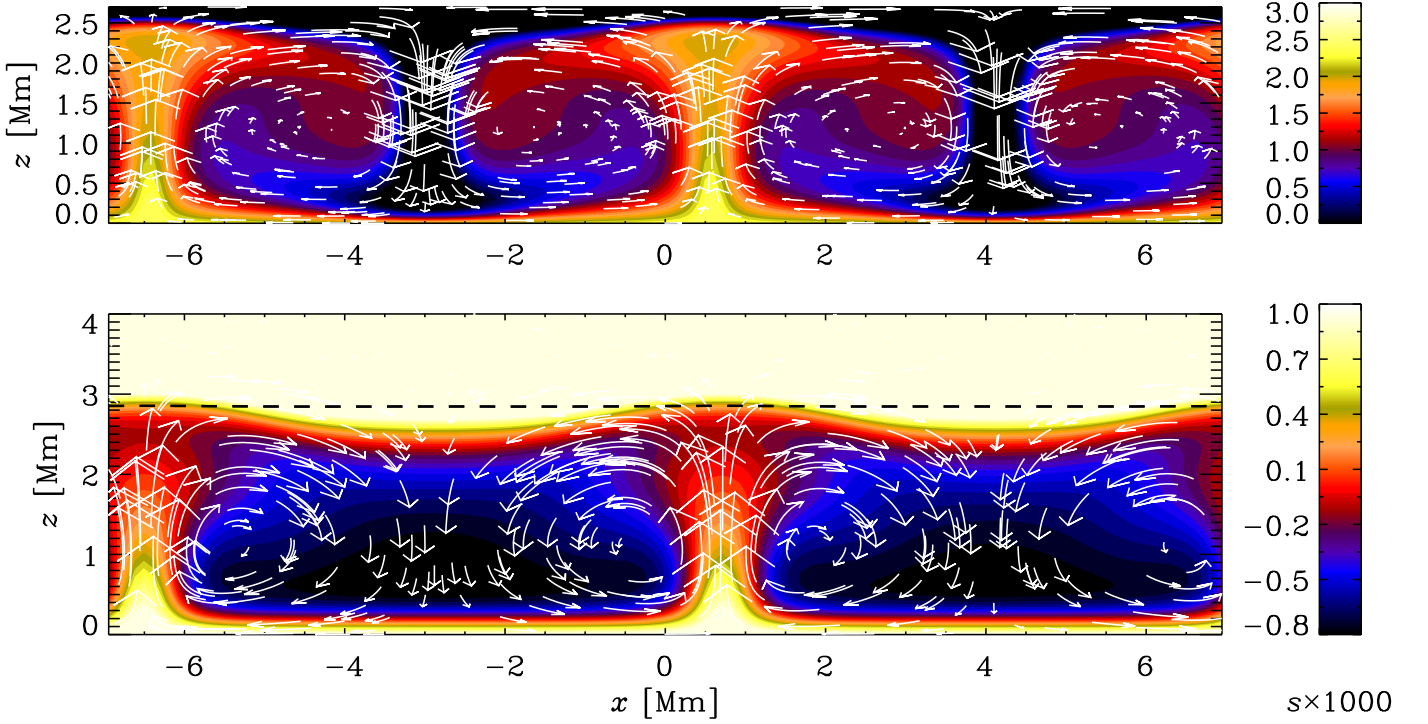


Fig. 12. Comparison of velocity and entropy distribution in two-dimensional convection using the optically thick approximation with a radiative upper boundary condition (upper panel) and radiative transfer (lower panel). In the lower panel, the dashed line gives the contour $\tau = 1$. In both cases we have $\text{Pr} = 100$ and the values of $\text{Ra} = 3.6 \cdot 10^4$. In the color bars, s has been multiplied by 1000. Note that the color table has been clipped toward high values so as not to show the strong increase of s above the $\tau = 1$ surface.

tically thick approximation. This corresponds to $\tilde{\kappa}_0 = 1.7 \cdot 10^4$, which is too small to obtain a proper polytropic lower part. Therefore we choose in the following $\text{Pr} = 100$, in which cases the critical value for the onset of convection is at $\mathcal{K} \gtrsim 0.02$ (corresponding to $\text{Ra} \lesssim 6600$).

In the following, we take $\mathcal{K} = 0.01$, so $\text{Ra} = 3.6 \cdot 10^4$, $d = 2.70 \text{ Mm}$, $\nu = 1.8 \text{ Mm km s}^{-1}$ (corresponding to $\nu = 1.8 \cdot 10^{13} \text{ cm}^2 \text{ s}^{-1}$), and $\tilde{\kappa}_0 = 3.4 \cdot 10^5 \text{ Mm}^{-1} \text{ cm}^3 \text{ g}^{-1}$; see the

Table 5. Summary of model parameters as a function of \mathcal{K} for $n = 1$.

\mathcal{K}	Pr Ra	d	χ_{mid}	K_0	$\tilde{\kappa}_0$
$5 \cdot 10^{-1}$	$7.5 \cdot 10^0$	0.63	$5.6 \cdot 10^{-1}$	$6.6 \cdot 10^{-6}$	$6.8 \cdot 10^3$
$2 \cdot 10^{-1}$	$7.1 \cdot 10^2$	1.31	$2.6 \cdot 10^{-1}$	$2.6 \cdot 10^{-6}$	$1.7 \cdot 10^4$
$1 \cdot 10^{-1}$	$7.7 \cdot 10^3$	1.73	$1.4 \cdot 10^{-1}$	$1.3 \cdot 10^{-6}$	$3.4 \cdot 10^4$
$5 \cdot 10^{-2}$	$5.9 \cdot 10^4$	2.08	$7.7 \cdot 10^{-2}$	$6.6 \cdot 10^{-7}$	$6.8 \cdot 10^4$
$2 \cdot 10^{-2}$	$6.6 \cdot 10^5$	2.46	$3.3 \cdot 10^{-2}$	$2.6 \cdot 10^{-7}$	$1.7 \cdot 10^5$
$1 \cdot 10^{-2}$	$3.6 \cdot 10^6$	2.70	$1.8 \cdot 10^{-2}$	$1.3 \cdot 10^{-7}$	$3.4 \cdot 10^5$
$5 \cdot 10^{-3}$	$1.9 \cdot 10^7$	2.89	$9.1 \cdot 10^{-3}$	$6.6 \cdot 10^{-8}$	$6.8 \cdot 10^5$
$2 \cdot 10^{-3}$	$1.5 \cdot 10^8$	3.11	$3.8 \cdot 10^{-3}$	$2.6 \cdot 10^{-8}$	$1.7 \cdot 10^6$
$1 \cdot 10^{-3}$	$6.9 \cdot 10^8$	3.24	$1.9 \cdot 10^{-3}$	$1.3 \cdot 10^{-8}$	$3.4 \cdot 10^6$
$5 \cdot 10^{-4}$	$3.1 \cdot 10^9$	3.35	$9.9 \cdot 10^{-4}$	$6.6 \cdot 10^{-9}$	$6.8 \cdot 10^6$
$2 \cdot 10^{-4}$	$2.2 \cdot 10^{10}$	3.47	$4.1 \cdot 10^{-4}$	$2.6 \cdot 10^{-9}$	$1.7 \cdot 10^7$
$1 \cdot 10^{-4}$	$9.5 \cdot 10^{10}$	3.55	$2.1 \cdot 10^{-4}$	$1.3 \cdot 10^{-9}$	$3.4 \cdot 10^7$

Notes. The values discussed and used in this paper are shown in bold face. All dimensional quantities have the units discussed in this paper.

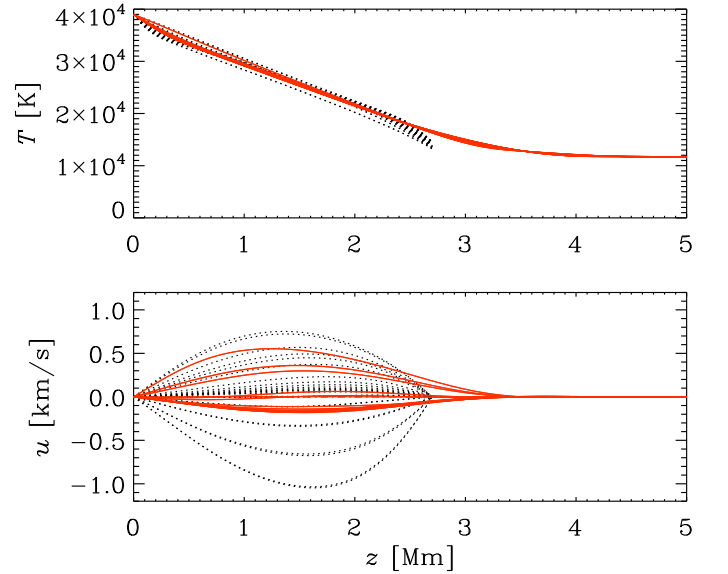


Fig. 13. Comparison of vertical temperature and velocity profiles at different x positions for the model shown in Figure 12.

sixth row of Table 5. We choose $L_x = 14 \text{ Mm}$, which is large enough to accommodate two convection cells into the domain; see Figure 12. The $\tau = 1$ surface in the radiative transfer calculation agrees approximately with the height expected from the optically thick models using a radiative upper boundary condition. In the radiative transfer calculation, the specific entropy

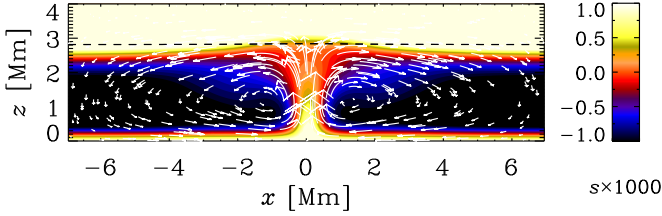


Fig. 14. Similar to the lower panel of Figure 12, but at a later time ($t = 500$ ks), when the solution has switched into a single-cell configuration.

increases sharply with height above the $\tau = 1$ surface. Note also that the characteristic narrow downdrafts of the optically thick calculation are now much broader when radiation transfer is used. Furthermore, the distinct entropy minimum near the surface is less pronounced in the latter case. This is because near $z = d$, the local value of χ is rather large (see the lower panel of Figure 11), so the thickness of the thermal boundary layer becomes comparable to d itself.

In the model using the diffusion approximation, the temperature variations are much larger than in the model with radiative transfer; see Figure 13. In the latter case, the velocities overshoot into the upper stably stratified layer, and are smaller than in the diffusion approximation by about a factor of two.

It turns out that the solution with radiative transfer shown in Figure 12 is quasi-stable until about 350 ks (≈ 4 days) and then switches into a single-cell configuration with a fairly isolated updraft; see Figure 14. We have seen similar behavior in other cases with radiation too, and it is possible that this is a consequence of our setup. Firstly, the restriction to two-dimensional convection is a serious artifact. Secondly, the assumption of a fixed temperature at the bottom was a mathematical convenience, but it is not physical motivated.

4. Increasing the density contrast

As alluded to in the introduction, the inclusion of the physics of radiation implies the occurrence of σ_{SB} as an additional physical constant that couples the resulting temperature and density contrasts to changes in the Rayleigh number. Given that we have already made other simplifications such as the negligence of hydrogen ionization, we end up with rather small density contrasts of less than ten, as seen in Table 4. By considering σ_{SB} an adjustable parameter, we can alleviate this constraint. We demonstrate this in Table 6, where we increase the value of σ_{SB} from its physical value of $5.67 \cdot 10^{-20} \text{ g cm}^{-3} \text{ km}^3 \text{ s}^{-3} \text{ K}^{-1}$ by eight orders of magnitude, keeping however K_0 fixed. We have chosen here $K_0 = 1.3 \cdot 10^{-7} = \text{g cm}^{-3} \text{ km}^3 \text{ s}^{-3} \text{ Mm K}^{-1}$, which corresponds to the model in the sixth row of Table 5. Since σ_{SB} enters the definition of \mathcal{K} , its value is now no longer constant, even though K_0 is. The Rayleigh numbers change slightly, because they depend on the values of density and temperature in the middle of the domain, which do of course change.

Large density contrasts are one of the important ingredients in modeling the physics of sunspot formation by surface effects such as the negative effective magnetic pressure instability; see Brandenburg et al. (2013) for a recent model. Including radiation into such still rather idealized models was indeed an important motivation behind the work of the present paper.

5. Conclusions

The inclusion of radiative transfer in a hydrodynamic code provides a natural and physically motivated way of placing an upper stably stratified layer on top of an optically thick layer that may be stably or unstably stratified. Which of the two depends on the opacity. Using a Kramers-like opacity laws with freely adjustable exponents on density and temperature yields polytropic solutions for certain combinations of the exponents a and b . The prefactor in the opacity law determines essentially the values of the Péclet and Rayleigh numbers. However, in contrast to earlier studies of convection in polytropic layers, the temperature contrast is no longer a free parameter and increases with increasing Rayleigh number—unless one considers the Stefan–Boltzmann ‘constant’ as an adjustable parameter. The physical values of the prefactor on the opacity are much larger than those used here, but larger prefactors lead to values of the radiative diffusivity that become eventually so small that temperature fluctuations on the mesh scale cannot be dissipated by radiative diffusion. In previous work (Nordlund, 1982; Steffen et al., 1989; Vögler et al., 2005; Heinemann et al., 2007; Freytag et al., 2012), this problem has been avoided by applying numerical diffusion or using numerical schemes that dissipate the energy when and where needed. However, this may also suppress the possibility of physical instabilities that we are ultimately interested in. This motivates the investigation of models with prefactors in the Kramers opacity law that are manageable without the use of numerical procedures to dissipate energy artificially.

It turns out that in all cases with a and b such that $n > -1$, the stratification corresponds to a polytrope with index n below the photosphere and to an isothermal one above it. This was actually expected given that such a solution has previously been obtained analytically in the special case of constant κ (corresponding to $a = b = 0$); see Spiegel (2006). On the other hand, the isothermal part was apparently not present in the simulations of Edwards (1990).

Comparing with realistic simulations of the Sun, there is not really an isothermal part, but a pronounced sudden drop in temperature followed by a continued decrease in temperature (see, e.g., Stein & Nordlund, 1998). On the other hand, in our simulations there is no jump in the temperature profile near the surface and the atmosphere changes smoothly from polytropic to isothermal. We suspect that the reason for this difference is that in our models ionization effects are ignored, while in the solar atmosphere the degree of ionization of hydrogen increases with depth. In the Sun, the density decreases significantly from the upper part of the convection zone as we go to the photosphere. This makes the opacity smaller and the atmosphere in the photosphere becomes transparent. At the height where the ionization temperature of hydrogen is reached, the H^- opacity becomes important, which is not included in our simulations. The radiative heat conductivity in our simulations is found to be constant

Table 6. Density contrast and other model parameters as a function of σ_{SB} for $n = 1$ and $K_0 = 1.3 \times 10^{-7}$.

σ_{SB}	Pr Ra	d	χ_{mid}	$\rho_{\text{bot}}/\rho_{\text{top}}$	$\tilde{\kappa}_0$
$5.67 \cdot 10^{-20}$	$3.63 \cdot 10^6$	2.70	$1.8 \cdot 10^{-2}$	3.2	$3.4 \cdot 10^5$
$5.67 \cdot 10^{-18}$	$9.45 \cdot 10^6$	3.55	$2.1 \cdot 10^{-2}$	10.0	$3.4 \cdot 10^7$
$5.67 \cdot 10^{-16}$	$1.23 \cdot 10^7$	3.82	$2.2 \cdot 10^{-2}$	31.6	$3.4 \cdot 10^9$
$5.67 \cdot 10^{-14}$	$1.33 \cdot 10^7$	3.90	$2.2 \cdot 10^{-2}$	100.0	$3.4 \cdot 10^{11}$
$5.67 \cdot 10^{-12}$	$1.36 \cdot 10^7$	3.93	$2.2 \cdot 10^{-2}$	316.2	$3.4 \cdot 10^{13}$

throughout the optically thick part and then increases sharply in the optically thin part. Solving this in the optically thick approximation, which has sometimes been done, becomes computationally expensive and even unphysical, so radiative transfer becomes a viable alternative for studying layers that are otherwise polytropic in the lower part of the domain.

Acknowledgements. We are indebted to Tobi Heinemann for his engagement in implementing the radiative transfer module into the PENCIL CODE. This work was supported in part by the European Research Council under the AstroDyn Research Project No. 227952, and by the Swedish Research Council under the project grants 621-2011-5076 and 2012-5797. We acknowledge the allocation of computing resources provided by the Swedish National Allocations Committee at the Center for Parallel Computers at the Royal Institute of Technology in Stockholm and the National Supercomputer Centers in Linköping, the High Performance Computing Center North in Umeå, and the Nordic High Performance Computing Center in Reykjavik.

Appendix A: Cooling rate and correction factor

The purpose of this appendix is to show that for one-dimensional temperature perturbations, the correct cooling rates are obtained with just two rays if the $D/3$ correction factor is applied. Similar considerations apply also to the case of two-dimensional problems. The situation is different from the case of general three-dimensional perturbations with wavevector \mathbf{k} (Spiegel, 1957). Within the framework of the Eddington approximation the cooling rate is (Unno & Spiegel, 1966; Edwards, 1990)

$$\lambda_{3D} = \frac{16\sigma_{SB}T^3}{\rho c_p} \frac{\kappa \rho \mathbf{k}^2}{3\kappa^2 \rho^2 + \mathbf{k}^2}. \quad (\text{A.1})$$

It is convenient to introduce here a photon diffusion speed as

$$c_\gamma = 16\sigma_{SB}T^3/\rho c_p \quad (\text{A.2})$$

and to write Equation (A.1) in the form

$$\lambda_{3D} = \frac{c_\gamma \ell \mathbf{k}^2/3}{1 + \ell^2 \mathbf{k}^2/3}, \quad (\text{A.3})$$

where $c_\gamma \ell/3 = \chi$ is the radiative diffusivity, as defined in Equation (23), and $\ell = 1/\kappa \rho$ is the local mean-free path of photons.

If we were to solve the transfer equation without correction factor, we would get Equation (A.3) without the two $1/3$ factors. This would evidently violate the well-known cooling rate $\chi \mathbf{k}^2$ in the optically thick limit, but in the optically thin limit it would be in agreement with Equation (A.3), because the two $1/3$ factors would cancel. However, we have to remember that temperature perturbations are assumed one-dimensional, so the intensity can only vary in the z direction, while the rays still go in all three directions. This means that under the sum in Equation (15) only one third of the $I - S$ terms give a contribution, and that the cooling rate is therefore

$$\lambda_{1D} = \frac{c_\gamma \ell k_z^2/3}{1 + \ell^2 k_z^2}, \quad (\text{A.4})$$

which has now only a single $1/3$ factor. Likewise, if we had two-dimensional perturbations such as in two-dimensional convection considered in Section 3.13, only $2/3$ of the terms under the sum in Equation (15) would contribute. However, in a two-dimensional radiative transfer calculation, the additional $1/3$ would be absent, which explains the $D/3$ correction factor with $D = 2$ in this case.

We have verified that with the correction factor in place, the code yields now the same cooling rates in both the optically thick

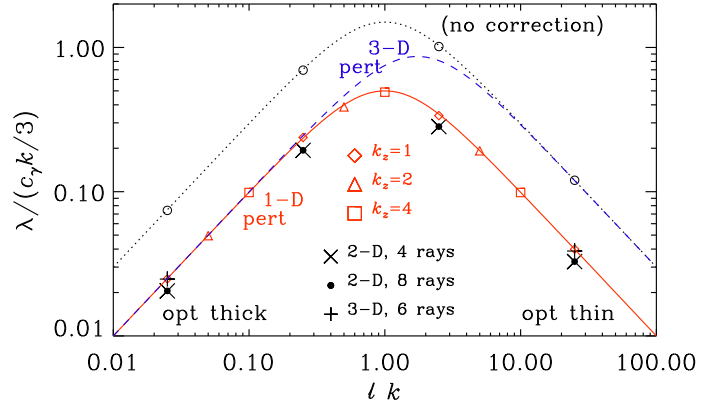


Fig. A.1. Dependence of the cooling rates computed from models with different values of κ_0 (from 10^2 to $10^5 \text{ Mm}^{-1} \text{ cm}^3 \text{ g}^{-1}$) and k_z ($=1, 2$, and 4 indicated by diamonds, triangles, and squares, respectively). 2-D models with 4 and 8 rays are indicated by crosses and circles, respectively, while 3-D models with 6 rays are shown as plus signs. The red solid line corresponds to Equation (A.4), the dashed blue line to Equation (A.3), and the dotted line with open circles to the case without correction factor.

and thin regimes, regardless of the numbers of rays used. This is shown in Figure A.1, where we plot cooling rates for different values of κ_0 in a domain of size 2π (in Mm), so the smallest wavenumber is 1 Mm^{-1} . With $\rho = 4 \times 10^{-4} \text{ g cm}^{-3}$ the photon mean-free path varies from 0.025 to 25 Mm^{-1} as κ_0 is decreased from 10^5 to $10^2 \text{ Mm}^{-1} \text{ cm}^3 \text{ g}^{-1}$. For the Kramers opacity, we use the exponents $a = 1$ and $b = 0$. (No gravity is included here, so there would be no convection.) The temperature is $38,968 \text{ K}$, as before, which yields $c_\gamma = 3.87 \text{ km s}^{-1}$ for the photon diffusion speed. There is excellent agreement between 1-D cases with correction factor and the 3-D calculation (with one-dimensional perturbation). However, the $2/3$ correction factor in the 2-D calculation (both with 4 and with 8 rays) seems to be systematically off and should instead be around 0.8 for better agreement. However, as discussed before, the correction factor does not affect the steady state and therefore also not the results presented in Section 3.13. The diffusion approximation would imply $\lambda = (c_\gamma k/3) \ell k = \chi k^2$, which corresponds to the diagonal in Figure A.1 and agrees with the red solid line for $\ell k \lesssim 0.5$.

References

- Brandenburg, A. 2005, *ApJ*, 625, 539
- Brandenburg, A., Jennings, R. L., Nordlund, Å., Rieutord, M., Stein, R. F., Tuominen, I. 1996, *J. Fluid Mech.*, 306, 325
- Brandenburg, A., Kleeorin, N., & Rogachevskii, I. 2013, *ApJL*, submitted, arXiv:1306.4915
- Cattaneo, F., Brummell, N. H., Toomre, J., Malagoli, A., Hurlburt, N. E. 1991, *ApJ*, 370, 282
- Edwards, J. M. 1990, *MNRAS*, 242, 224
- Gastine, T., & Dintrans, B. 2008, *A&A*, 484, 29
- Freytag, B., Steffen, M., Ludwig, H.-G., Wedemeyer-Böhm, S., Schaffnerberger, W., & Steiner, O. 2012, *J. Comput. Phys.*, 231, 919
- Heinemann, T., Dobler, W., Nordlund, Å., & Brandenburg, A. 2006, *A&A*, 448, 731
- Heinemann, T., Nordlund, Å., Scharmer, G. B., Spruit, H. C. 2007, *ApJ*, 669, 1390
- Käpylä, P. J., Mantere, M. J., & Brandenburg, A. 2012, *ApJ*, 755, L22
- Käpylä, P. J., Mantere, M. J., Cole, E., Warnecke, J., & Brandenburg, A. 2013, *ApJ*, submitted, arXiv:1301.2595

- Miesch, M. S., Elliott, J. R., Toomre, J., Clune, T. L., Glatzmaier, G. A., & Gilman, P. A. 2000, *ApJ*, 532, 593
- Nordlund, Å. 1982, *A&A*, 107, 1
- Nordlund, Å. 1985, *Solar Phys.*, 100, 209
- Spiegel, E. A. 1957, *ApJ*, 126, 202
- Spiegel, E. A. 2006, *EAS Publ. Ser.*, 21, 127
- Steffen, M., Ludwig, H.-G., & Krüß, A. 1989, *A&A*, 123, 371
- Stein, R. F., & Nordlund, Å. 1989, *ApJ*, 342, L95
- Stein, R. F., & Nordlund, Å. 1998, *ApJ*, 499, 914
- Stein, R. F., & Nordlund, Å. 2012, *ApJ*, 753, L13
- Unno, W., & Spiegel, E. A. 1966, *Publ. Astron. Soc. Japan*, 18, 85
- Vögler, A., Shelyag, S., Schüssler, M., Cattaneo, F., & Emonet, T. 2005, *A&A*, 429, 335
- Stix, M. 2002, *The Sun: an introduction* (Springer-Verlag, Berlin)